RSC Advances

PAPER

View Article Online
View Journal | View Issue

Cite this: *RSC Adv.*, 2023, **13**, 4523

Synthesis of copper–silver–zinc oxide nanocomposites for 4-nitrophenol reduction: doping and heterojunction†

Buzuayehu Abebe, * Bontu Kefale and Dereje Tsegaye Leku*

The charge transfer and visible-light absorption capacities of stable materials are crucial in several applications, such as catalysis, absorption, sensors, and bioremediation. Copper–silver–zinc oxide nanocomposites (NCs) were synthesized using PVA as a capping agent and urea as a stabilizing agent. DTG analysis confirmed 500 °C was the optimum temperature for the total decomposition of PVA after capping the nanoparticles (NPs) to yield a pure composite. The XRD analysis showed the presence of copper inclusions in the ZnO lattice and the formation of Ag and CuO heterojunctions with ZnO. The photoluminescence (PL) analysis confirmed the more significant visible light absorption and charge transfer properties of the composite compared to those of single ZnO NPs. Foam-type porosity occurred during gas evolution at many of the points shown in the SEM/TEM images. Slight lattice fringe differences between the composite and ZnO NPs due to copper inclusion were confirmed from the HRTEM image and XRD pattern analysis. The crystallinity of the NPs and NCs was confirmed by the XRD pattern and SAED analysis. The diffusion-controlled charge transfer process was witnessed through CV electrochemical analysis. Thus, the energy- and time-efficient solution combustion synthesis (SCS) approach has a crucial future outlook, specifically for an industrial, scalable application. The NCs demonstrated more potential than ZnO NPs in an organic catalytic reduction reaction of 4-nitrophenol to 4-aminophenol.

Received 8th December 2022
Accepted 30th January 2023

DOI: 10.1039/d2ra07845g

rsc.li/rsc-advances

1. Introduction

Human health is negatively impacted by the contamination of water caused by the emission of hazardous organic pollutants like 4-nitrophenol (4-NP).[1] 4-NP is employed in a variety of fields, including the manufacturing of a number of materials, as an indicator, and as a corrosion inhibitor. So far, the largest advancements have been made in the catalytic reduction of the hazardous 4-nitrophenol to the less hazardous 4-aminophenol (4-AP) on a catalyst surface, specifically employing sodium borohydride as a reducing agent.[1,2] An emerging technology, nanotechnology, offers to produce heterogeneous catalyst nanomaterials, which is crucial in different applications.[3,4] Nanoscale-sized zinc oxide (ZnO) is a potential semiconductor material that exhibits superior properties due to its chemical stability, environmental friendliness, and novel catalytic properties, although with some drawbacks such as low surface area, photocorrosion, and electron–hole recombination.[5,6] The doping and forming a heterojunction with different bandgap materials such as silver and copper address the ZnO drawbacks.[5,7] Doping is either substitutional or interstitial insertion of the dopant in the host lattice, resulting in tuning the optical, electrical, and magnetic properties. The hard and soft (Lewis) acids and bases (HSAB) theory is crucial for regulating the host-dopant reactivity balance.[8,9] The heterojunction is a band alignment between two or more semiconductors with different band gaps. Heterojunction between semiconductors boosts the surface area, charge transfer, and optoelectrical properties. The charge transfer process reduces electron–hole recombination, which is critical for several applications, such as catalysis and photocatalysis.[10] The coupling of noble metals such as silver allows for light–matter interaction, which improves visible light absorption and charge transfer properties due to the formation of a Schottky barrier. Forming a heterojunction between ZnO and CuO also assists the charge transfer process within the interface[5,11]

Recently, some silver and copper doped ZnO NCs works were reported.[5,7,12] Xu *et al.* described the formation of Ag/Cu–ZnO heterojunction synthesized from the zinc-/copper-acetate and silver nitrate precursors by the sol–gel method. The synthesized materials showed enhanced charge transfer and better visible light absorption capacity compared to ZnO NPs, which also showed direct effect on the dye degradation potential.[7] Manjari *et al.* reported Cu–Ag NPs decorated ZnO composites by green synthesis method for electrochemical sensor and pollutant

Adama Science and Technology University, Department of Applied Chemistry, Adama, 1888, Ethiopia. E-mail: buzea8@gmail.com; detsegaye@gmail.com

† Electronic supplementary information (ESI) available. See DOI: https://doi.org/10.1039/d2ra07845g

reduction/degradation applications. The synthesized composites showed enhanced catalytic and sensing capacity due to the synergistic effect of Cu–Ag NPs with ZnO.[12] Xu *et al.* synthesized Ag/CuO/ZnO heterostructure composite by chemical- and photochemical-deposition methods. The synthesized composite showed improved methyl orange and Rhodamine B degradation capacity compared to the single ZnO. The enhanced degradation capacity of the composites is due to enhancement in the surface area, charge transfer, and visible light absorption capacity than ZnO.[5] Besides, using the co-precipitation method, the Ag-decorated copper-doped ZnO microcrystal was synthesized by Wan and his groups. The copper ion was used as a dopant and morphology controller in this study. The synthesized Ag-decorated copper-doped ZnO microcrystals showed superior photocatalytic activity compared to single ZnO as a result of intensive light absorption improvement and Schottky barrier formation.[13] Here in the aforementioned studies, materials properties improvement as a result of doping/heterojunction was well reported. However, the doping interpretation, specifically based on the XRD pattern peak shift was scarce. Besides, the energy-/time-efficient solution combustion synthesis (SCS) approach based on the critical LaMer's nanocrystal development model and HSAB host-dopant reactivity balance theory was not reported.

This study gives insight into the chemistry of doping and heterojunction on the silver–copper–zinc oxide NCs material synthesized by the SCS approach. The chemistry of doping and heterojunction is interpreted based on LaMer's nanocrystal development model and HSAB host-dopant reactivity balance theory. As confirmed by the XRD pattern and HRTEM analysis, the SCS approach allows the reduction of silver NPs to form a heterojunction with ZnO without inclusion in the ZnO lattice. However, copper was doped in the ZnO lattice as-well-as form a heterojunction. Thus, the copper-doped ZnO and silver–copper oxide–zinc oxide heterojunction (Cu–ZnO/CuO/Ag) is the synthesized NCs materials. The SEM/TEM image confirmed the occurrence of greater porosity for NCs than ZnO. The doping and heterojunction-induced charge transfer and visible light absorption capacity of NCs than ZnO were confirmed from PL analysis. The overall characterization improvement towards NCs compared to the ZnO NPs were proved on catalytic reduction of 4-NP to 4-AP. This investigation confirmed that NCs had a higher catalytic reduction capacity than ZnO NPs, just within 210 seconds. In this regard, the SCS is a promising approach for producing a porous and catalytically efficient material within a short time and using less energy.

2. Experimental

2.1. Reagents and chemicals

The reagents and chemicals that are employed are silver nitrate ($AgNO_3$, 99%), copper(II) nitrate trihydrate ($Cu(NO_3)_2 \cdot 3H_2O$, 99%), zinc nitrate ($Zn(NO_3)_2 \cdot 6H_2O$, 99.5%), polyvinyl alcohol ([–CH_2CHOH–]n, Mw: 85 000–124 000), urea (CH_4N_2O, 99.0%), and distilled water. The chemicals and reagents were employed immediately after purchase without further purification.

2.2. Synthesis of NPs and NCs

The NPs and NCs were synthesized by forming a complex between metal precursors and the fuel/surfactant. The procedures were adopted by combining the previous reports[14,15] with slight modifications. In detail, the ternary composites were synthesized by mixing a stoichiometric amount of silver, copper, and zinc salt precursors in 5 : 5 : 90 ratios (5% silver, 5% copper, and 90% zinc salts), respectively, in 50 mL of poly(vinyl alcohol) (PVA)-distilled water solution. The PVA-distilled water solution was prepared by dissolving 1 g of the PVA polymer in hot distilled water (80 °C) for about 20 minutes. The nitrate salt precursor is the best choice due to its novel solubility, oxidizing properties, and stability.[16,17] Herein, the host-dopant reactivity balance was selected based on the hard and soft acids and bases (HSAB) theory.[8,9] The mixture was dissolved at a reduced temperature (50 °C) by continuously stirring on the hot plate-magnetic stirrer for about 15 minutes.

During the dissolution of the salt precursor, a stoichiometric amount (0.158 mol L^{-1}) of CH_4N_2O was continuously added from the burette. The dissolved mixture was dehydrated by raising the hot plate temperature in the range of 90–115 °C for about 4–5 hours. The dry precursor fuel/surfactant gel temperature then further increased to the approximate complex ignition temperature range of 160–260 °C within 15–25 minutes. Finally, the combusted foam-type by-product was crushed to powder and calcined at 500 °C for three hours. 500 °C is the temperature at which PVA decomposed completely after stabilizing the NPs, which is optimized on the TGA-DTA analysis. The single silver metal, copper oxide, and zinc oxide NPs were also synthesized by following similar procedures except for adding an appropriate amount of each salt precursors.

2.3. Catalytic reduction of 4-NP

The 4-NP to 4-AP reduction procedures on the surface of NPs and NCs were adapted from a recent study.[18] To give a rich yellow color, 1.10 mL of 0.01 M (1.1×10^{-4} M) 4-NP was mixed with 0.38 g/100 mL (0.1 M) of excess sodium borohydride ($NaBH_4$). In this case, $NaBH_4$ was used to reduce 4-NP to the 4-nitrophenolate ion. After adding 10 mg of the catalyst to the mixture, a UV-vis spectrophotometer (P9 UV/Visible double-beam spectrophotometer) was used to track the conversion of 4-NP to 4-AP.

2.4. Characterization

The TGA-DTA technique (DTG, DTG-60H) was used to characterize the thermal stability of NPs and NCs in a nitrogen atmosphere at a flow rate of 20.0 mL min^{-1} and a ramp temperature of 50 °C min^{-1}. The materials' crystallinity was studied by XRD pattern analysis (XRD-7000, Shimadzu), at a voltage of 40.0 kV, a current of 30.0 mA, and a scan speed of 3.0 deg min^{-1}. The materials' optical properties were characterized by photoluminescence (PL) spectroscopic techniques (Agilent, Eclipse fluorescence spectrophotometer). The scanning electron microscope (SEM) (JCM-6000Plus) and transmission electron microscopy (TEM) (JEOL TEM 2100 HRTEM)

techniques were used to understand the morphological characteristics. The compositional analysis of the materials was characterized by energy-dispersive X-ray (EDAX) analysis. Materials' electrochemical properties were analyzed by cyclic voltammetry (with a CH 660E potentiostat, an electrochemical analyzer) in a three-electrode system. The catalyst paste is formed by mixing silicon oil, graphite powder, and NPs/NCs in 3 : 14 : 3 ratios. The NPs and NCs paste, Ag/AgCl, and platinum wire were used as working, reference, and counter electrodes, respectively. The UV-vis spectrophotometer (P9 UV/Visible double-beam spectrophotometer) was used to control the 4-NP reduction to 4-AP.

3. Results and discussion

3.1. Characterizations

The materials stability and appropriate calcination temperature selection were done by the TGA-DTA analysis. Fig. 1 shows the DTG spectra for the PVA-ZnO composite before calcination. Mainly two decompositions processes took-place; the first decomposition occurred in the temperature range of 135–215 °C is due to the surface or/and interstitial/crystal absorbed water molecules.

The second decomposition, which occurred in the temperature range of 305–505 °C is as a result of PVA polymer total degradation.[15]

The purity and crystallinity of PVA polymer, NPs, and NCs were understood by XRD pattern analysis, as shown in Fig. 2(a). The XRD pattern analysis show 2θ peaks for raw PVA at 19.4 corresponding to the (101) plane of the crystal lattice (JCPDS, File No. 00-053-1847).[19] After calcination, no PVA and additional impurity XRD peaks were detected on the NPs and NCs. The absence of additional peak indicates the total decomposition of PVA and impurities during calcination at 500 °C. The single ZnO XRD pattern showed 2θ peaks corresponding with a hexagonal phase of wurtzite ZnO (JCPDS, File No. 00-036-1451).[20]

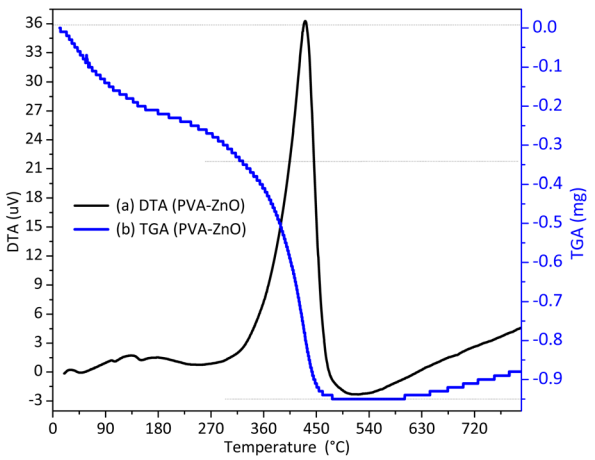

Fig. 1 TGA-DTA thermograms: the thermal decomposition behavior of poly(vinyl alcohol)/fuel–zinc nitrate complex; the two decomposition points are due to the surface/crystal adsorbed water molecules and total decomposition of PVA polymer.

The XRD pattern for single copper(II) oxide and silver metal shows a monoclinic (JCPDS, File No. 00-048-1548)[21] and face-centered-cubic (JCPDS, File No. 00-004-0783) phase,[22] respectively. The XRD pattern of doped composites showed additional peaks for silver metal and copper oxide. The detected additional peak reveals the availability of separate silver and copper oxide crystallites. This is probably by forming a heterojunction with ZnO (see Fig. 2(b)). However, the composites XRD pattern showed higher angle shift compared to the single ZnO (Fig. 2(c)), which reveals the presence of doping in addition to the heterojunction. In general, silver is reduced by reducing gaseous products such as hydrogen and ammonia during combustion.[14,23] Thus, the shift is probably due to the interstitial inclusion of copper dopant in the ZnO lattice.[24] The XRD pattern analysis confirms the formation of Cu-doped ZnO/Ag/CuO (Cu–ZnO/Ag/CuO) NCs. The general host-dopant reaction of the complex during combustion is given in eqn (1), where z is the amount of dopant and ρ is the oxygen spillover valence.[25] The crystal structure of silver, copper oxide and zinc oxide, which developed from the American mineralogist crystal structure database (AMCSD), CIF data, is depicted in Fig. 2(d). The crystal structure is drawn using the visualization for electronic structural analysis (VESTA) software.

$$z\mathrm{Cu(NO_3)_2{\cdot}3H_2O} + (1 - z)\mathrm{Zn(NO_3)_2{\cdot}6H_2O} + \mathrm{PVA/oxidant} \rightarrow \mathrm{Cu_zZn_{(1-z)}O_{(2-\rho)}} + \text{gaseous products} \quad (1)$$

The optical properties of as-synthesized NPs and NCs were characterized by photoluminescence (PL) spectroscopic technique (Agilent, eclipse fluorescence spectrophotometer), as shown in Fig. 3(a). The first intense near-band edge transition peak detected at a wavelength of 396 nm is a result of photon-induced electron–hole recombination. The other peaks detected in the visible region are due to extrinsic and intrinsic defects.[26] The composite's PL spectra show intensity reduction compared to single ZnO spectra, which indicates the reduction of the photon-induced electron–hole recombination process.[27] The process of diminishing the electron–hole recombination has valuable benefits in different applications, such as photocatalysis, and the production of the hydroxyl radical, an oxidizing agent, due to the reaction of oxygen and water with electron and hole.[5,7] The NPs and NCs spectra were further deconvoluted to see the effects of light absorption capacity, as shown in Fig. 3(b and c), respectively. The visible light absorption capacity of the composite increased more than ZnO (see the pink ellipse curve). The violet and blue emissions are increased for NCs as the UV emission decreases. This visible light absorption enhancement for the NCs results from the development of doping or/and heterojunction between metal/metal oxides.

The materials' morphology, crystallinity, and porosity are understood from the SEM and TEM image analysis, as shown in Fig. 4–6. Fig. 4 shows the SEM images of ZnO NPs and composite (at 20 nm scale bar). The composite showed better porosity than single ZnO. The greater porosity of the composite

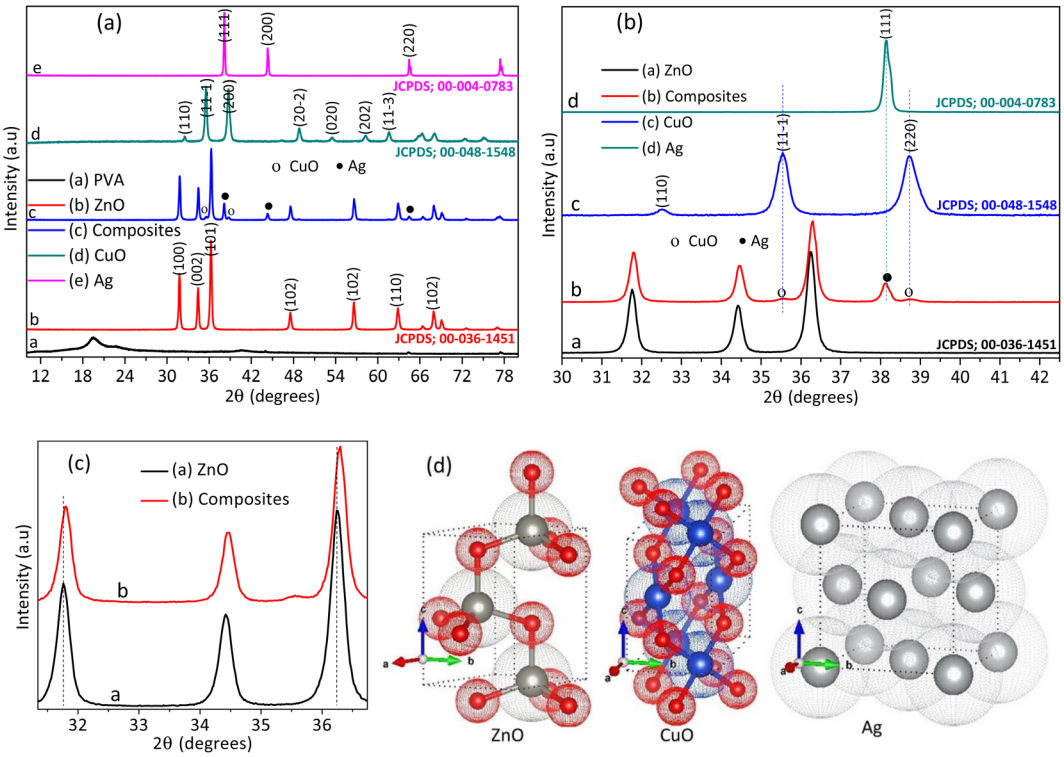

Fig. 2 The XRD pattern: (a) the XRD pattern for raw PVA polymer, zinc oxide, silver, copper oxide, and silver–copper–zinc composites, (b and c) the magnified view of 2(a), except the PVA XRD pattern. Herein, the occurrence of independent copper and silver peak on the composite XRD pattern indicates the presence of their independent crystal. The higher 2θ shift for the composite confirm inclusion of copper in the ZnO lattice, (d) the crystal structure of silver, copper oxide, and zinc oxide was developed from the AMCSD, CIF data, using VESTA software.

may confirm the formation of better fuel/surfactant complexes within the composite salt precursors than the zinc precursor alone. The respective inset image in Fig. 4(a) and (b) are the magnified images at 5 nm scale bar. The morphology of the composites has a spongy, foam-type morphology, which indicates the gas evolution is from many points.[28] The EDAX analysis was used to confirm the presence of an expected elemental composition of Zn, Ag, Cu, and O as prominent peaks at around 1, 3, 0.9, and 0.5 keV, respectively (Fig. S1†). The standard employed during analysis is likely to blame for the presence of elemental carbon. The probable source for elemental nitrogen is urea decomposition. The obtained weight percent and atomic percent compositional analysis findings are displayed in the inset table of Fig. S1.†

The pore generation during gaseous product evolution was further confirmed from the TEM image, as shown in Fig. 5(a) and 6(a) (red arrows). The lattice fringes of ZnO NPs and composite were calculated from the HRTEM images (Fig. 5(b) and 6(b), respectively). The slight lattice fringe value differences between ZnO NPs (0.265 nm) and composite (0.260 nm) are probably due to the inclusion of copper in the ZnO lattice, which is due to the slight crystal distortion.[29,30] The bright spots

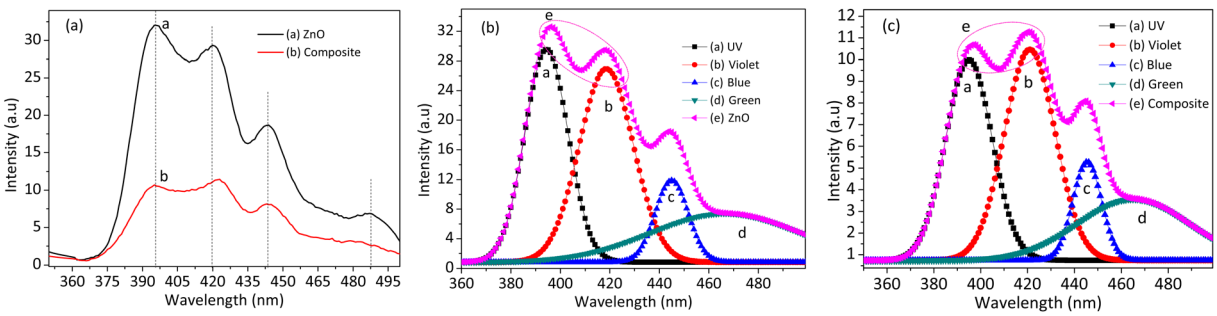

Fig. 3 PL spectra: (a) the optical properties analysis spectra for zinc oxide and silver–copper–zinc composite, (b and c) the deconvoluted zinc oxide and silver–copper–zinc composite spectra, respectively. The intensity reduction for the composites than ZnO indicates a reduction in the electron–hole recombination process. The deconvoluted spectra for the composite show intensity reduction than zinc oxide (see the ellipse curve), which confirms its greater visible light absorption capacity.

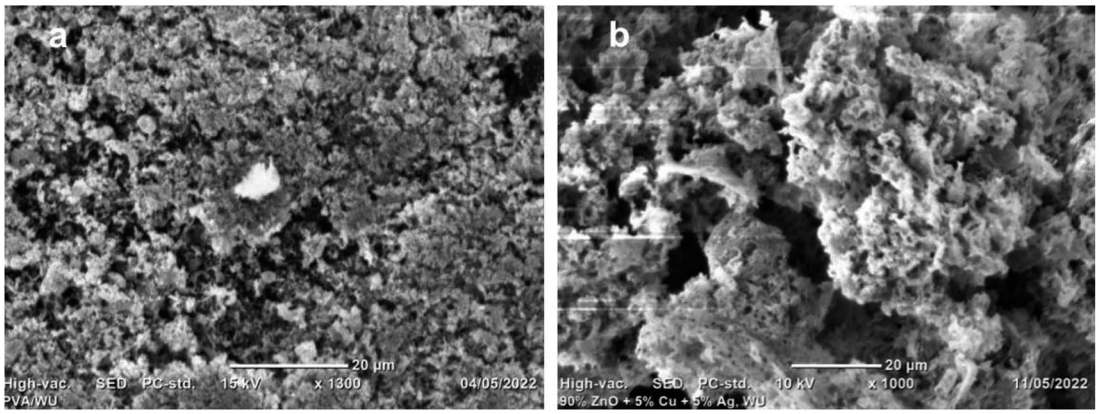

Fig. 4 SEM images: SEM morphological analysis images of (a) zinc oxide and (b) silver–copper–zinc composite. The composite SEM image showed greater porosity, probably the enhanced combustion and gas evolution ability of copper and silver precursors in the presence of fuel/surfactant.

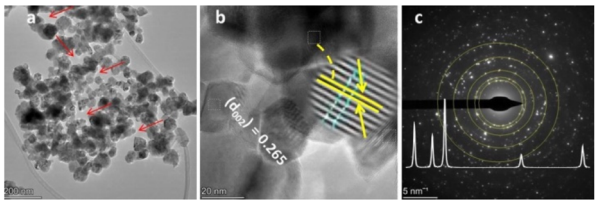

Fig. 5 TEM/HRTEM/SAED images: (a) TEM image, (b) HRTEM image (the inset is the fast Fourier transform pattern), (c) SAED ring (the inset is its XRD pattern) for zinc oxide. Some pores were observed on the TEM image, probably due to gas evolution (see the red arrows). The *d*-spacing value is corresponding to (002) plane of zinc oxide. The circle and bright spots on the SAED ring indicates the crystal plane and crystallinity of zinc oxide, respectively.

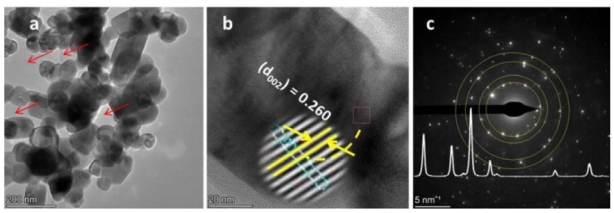

Fig. 6 TEM/HRTEM/SAED images: (a) TEM image, (b) HRTEM image (the inset is the fast Fourier transform pattern), (c) SAED ring (the inset is its XRD pattern) for silver–copper–zinc composite. Pores were observed on the TEM image, probably due to gas evolution (see the red arrows). The *d*-spacing value here also corresponds to the (002) plane of zinc oxide. The circle and bright spots on the SEAD ring indicate the crystal plane and crystallinity of the silver–copper–zinc composite, respectively.

on the SAED rings of NPs and NCs show their crystallinity (Fig. 5(c) and 6(c)). The diffraction rings on the ZnO NPs confirm its crystal planes, consistent with XRD interpretation. However, the SAED ring detected for the NCs is not as good as that of the NPs, probably due to crystal lattice distortion during interstitial copper inclusion.[24]

The electrochemical properties of the NPs and composites were analyzed by cyclic voltammetry (with CH 660E potentiostat, an electrochemical analyzer) in a three-electrode system, as shown in Fig. 7. Fig. 7(a) shows the cyclic voltammogram for ZnO NPs, in which no visible redox peak was detected. However, the cyclic voltammogram for the composites has reversible

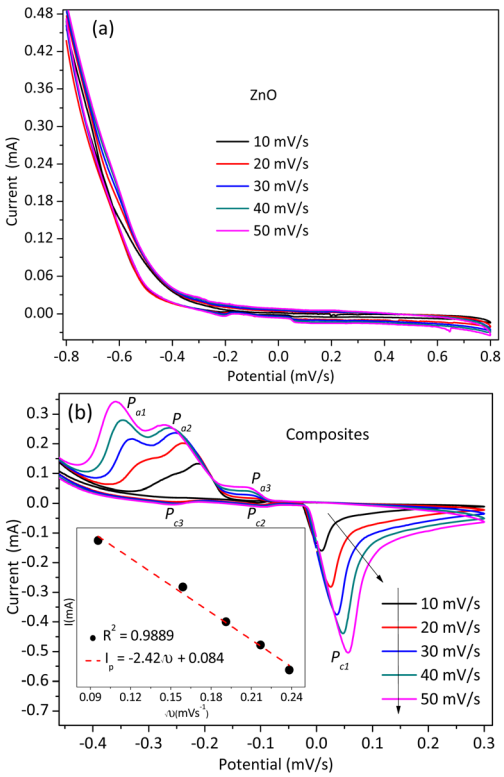

Fig. 7 The CV voltammogram: the CV analysis for (a) zinc oxide and (b) silver–copper–zinc composite: the inset is peak current *versus* square root of potential linear plot. No clear redox peak was detected for zinc oxide, and there is a redox peak for the composites, indicating proton intercalation and de-intercalation due to porosity. The fitting of the linear plot indicates diffusion-controlled charge transfer processes.

reduction and oxidation peaks (Fig. 7(b)). The oxidation/anodic (P_{a1}) and reduction/cathodic (P_{c1}) peaks are observed at different peak potential points. These potential peaks indicate the presence of an improvement in the electronic conductivity and catalytic properties of the NCs over the ZnO NPs.[31] These reversible redox peaks of the composites result from the material porosity. The porous nature of the materials facilitates charge intercalation and de-intercalation processes.[32] The shifting of the potential with increasing scan rate (from 10–50 mV s^{-1}) and the well-fitting of the peak current *versus* square root of the potential linear plot (see Fig. 7(b) inset) indicates the free diffusion of species without adsorption and the diffusion-controlled charge transfer processes, respectively.[31,33]

3.2. 4-NP catalytic reduction

Fig. 8 depicts the NPs- and NCs-catalyzed organic catalytic reduction process of 4-NP to 4-AP in the presence of $NaBH_4$ as a reducing agent. According to Fig. S2,† the greatest wavelength peak of the 4-NP is at about 316 nm. Then, the 4-nitrophenolate ion peak at 400 nm is created when 4-NP reacts with $NaBH_4$, which causes the 4-NP peak to completely vanish at 316 nm. Then, when 4-NP reacts with the catalyst, the 4-nitrophenolate ion is reduced and converted to 4-AP, which causes the creation of a new peak with a maximum wavelength value of 299 nm. The isotope points (marked by arrows) show a conversion process without any undesirable byproducts.[34] During the reaction, the 4-AP, 4-nitrophenolate ion, and 4-NP exhibit colorless, deep yellow, and yellow colors, respectively. On the 4-NP, the NCs demonstrated quick and effective reduction potential in just 210 seconds, compared to the ZnO NPs.

Using recently available literature,[1,2,35] the probable mechanism for the 4-NP catalytic reduction process to 4-aminophenol was suggested. First, a small number of bubbles appear when $NaBH_4$ is added to water as a result of hydrogen production; this is a reduction reaction between water and $NaBH_4$. A metal hydride complex then forms during the catalyst's addition. More bubbles develop during this catalyst addition step, most likely as a result of increased hydrogen production. At the same time, 4-NP adsorbed on the catalyst surface, and hydrogen transferred from the catalytic hydride complex to 4-NP (Fig. 9). Based on the mass spectrometry and density functional theory analyses, Kong *et al.* described in detail the processes of hydrogen absorption, the production of water molecules, and

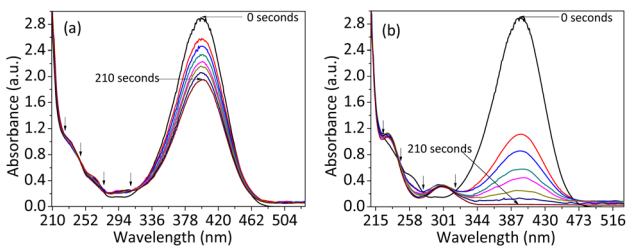

Fig. 8 4-NP catalytic reduction plots of (a) ZnO NPs and (b) silver–copper–zinc composite: The NCs show complete reduction of the 4-nitrophenol to the 4-aminophenol within 210 seconds.

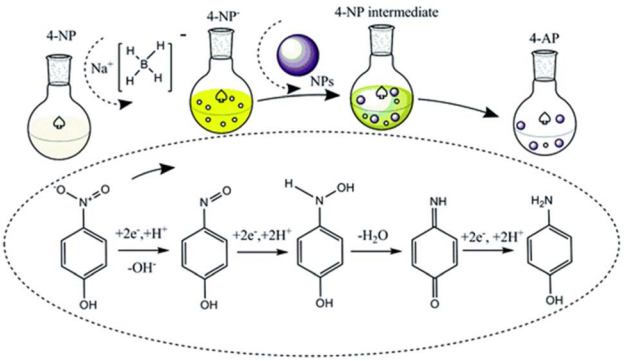

Fig. 9 Possible understanding of the conversion of 4-nitrophenol to 4-aminophenol using $NaBH_4$ and metal NPs as an H_2 source and catalyst, respectively. Reproduced/Adapted from ref. 1 with permission from The Royal Society of Chemistry.

their elimination by a sequential hydroxyl dehydration process.[35] The 4-nitrophenolate ion peak at 400 nm then gradually diminished, and the 4-AP peak at 299 nm progressively emerged. The 4-hydroxyl aminophenol transition state occurred during the 4-nitrophenolate ion-to-4-AP reduction process.[2] The entire conversion of the 4-NP ion to the 4-AP ion is shown by the creation of a colorless solution. In the end, 4-AP desorption takes place, which helps with catalyst recycling.

4. Conclusions

Thus, the combustion synthesis approach produced pure porous nanoscale-sized (30–70 nm) Cu-doped ZnO/CuO/Ag NCs. The material porosity resulted from gaseous product ejection during the combustion of the complex formed between the fuel/PVA and metal precursors. The XRD pattern analysis confirmed the doping and heterojunction formation. The SEM and TEM image analysis show the generated foam-type pores of the materials. The slight *d*-spacing differences between the NPs and composites are due to copper inclusion in the ZnO host. The PL analysis clearly showed the presence of charge transfer and visible light absorption improvement for the composites than single ZnO. The CV analysis reveals the diffusion-controlled type charge transfer process. Compared to the ZnO NPs, the copper–silver–zinc oxide NCs showed a much better reduction of 4-nitrophenol to 4-aminophenol.

Author contributions

Writing – original draft and Investigation by Buzuayehu Abebe. Laboratory work by Bontu Kefale the writing – review & editing by Dereje Tsegaye. All authors read in detail and approved the final manuscript.

Conflicts of interest

There are no conflicts to declare.

Acknowledgements

This study was supported by the Adama Science and Technology University (grant no. ASTU/AS-R/052/2022).

Notes and references

1 Y. R. Mejía and N. K. Reddy Bogireddy, *RSC Adv.*, 2022, **12**, 18661–18675.
2 Z. Wang, R. Su, D. Wang, J. Shi, J.-X. Wang, Y. Pu and J.-F. Chen, *Ind. Eng. Chem. Res.*, 2017, **56**, 13610–13617.
3 B. C. Hodges, E. L. Cates and J.-H. Kim, *Nat. Nanotechnol.*, 2018, **13**, 642–650.
4 X. Hai, S. Xi, S. Mitchell, K. Harrath, H. Xu, D. F. Akl, D. Kong, J. Li, Z. Li, T. Sun, H. Yang, Y. Cui, C. Su, X. Zhao, J. Li, J. Pérez-Ramírez and J. Lu, *Nat. Nanotechnol.*, 2022, **17**, 174–181.
5 K. Xu, J. Wu, C. F. Tan, G. W. Ho, A. Wei and M. Hong, *Nanoscale*, 2017, **9**, 11574–11583.
6 S. Mustapha, J. O. Tijani, M. M. Ndamitso, S. A. Abdulkareem, D. T. Shuaib, A. K. Mohammed and A. Sumaila, *Sci. Rep.*, 2020, **10**, 13068.
7 M. Xu, Y. Chen, W. Y. Hu, Y. T. Liu, Q. P. Zhang, H. Yuan, X. Y. Wang, J. X. Zhang, K. Y. Luo, J. Li and G. Xiong, *J. Phys. D: Appl. Phys.*, 2020, **53**, 025106.
8 R. Buonsanti and D. J. Milliron, *Chem. Mater.*, 2013, **25**, 1305–1317.
9 B. Abebe and H. C. A. Murthy, *RSC Adv.*, 2022, **12**, 5816–5833.
10 T. L. Yusuf, B. O. Orimolade, D. Masekela, B. Mamba and N. Mabuba, *RSC Adv.*, 2022, **12**, 26176–26191.
11 J. Yu, S. Zhuang, X. Xu, W. Zhu, B. Feng and J. Hu, *J. Mater. Chem. A*, 2015, **3**, 1199–1207.
12 G. Manjari, S. Saran, S. Radhakrishanan, P. Rameshkumar, A. Pandikumar and S. P. Devipriya, *J. Environ. Manage.*, 2020, **262**, 110282.
13 X. Wan, X. Liang, C. Zhang, X. Li, W. Liang, H. Xu, S. Lan and S. Tie, *Chem. Eng. J.*, 2015, **272**, 58–68.
14 Y. Gao, F. Meng, X. Li, J. Z. Wen and Z. Li, *Catal. Sci. Technol.*, 2016, **6**, 7800–7811.
15 B. Liu, Y. You, H. Zhang, H. Wu, J. Jin and H. Liu, *RSC Adv.*, 2016, **6**, 110349–110355.
16 S. J. Kim, S. Yoon and H. J. Kim, *Jpn. J. Appl. Phys.*, 2014, **53**, 02BA02.
17 B. Abebe, D. Tsegaye and H. C. Ananda Murthy, *RSC Adv.*, 2022, **12**, 24374–24389.
18 H. M. Ali, S. M. Ibrahim, E. F. Abo Zeid, A. F. Al-Hossainy and M. A. El-Aal, *RSC Adv.*, 2022, **12**, 16496–16509.
19 J. Selvi, S. Mahalakshmi, V. Parthasarathy, C. Hu, Y. Lin, K. Tung, R. Anbarasan and A. A. Annie, *Polym. Compos.*, 2019, **40**, 3737–3748.
20 F. Paraguay-Delgado, L. A. Hermida-Montero, J. E. Morales-Mendoza, Z. Durán-Barradas, A. I. Mtz-Enriquez and N. Pariona, *RSC Adv.*, 2022, **12**, 9898–9908.
21 Y.-T. Kwon, Y.-S. Kim, S. Kwon, M. Mahmood, H.-R. Lim, S.-W. Park, S.-O. Kang, J. J. Choi, R. Herbert, Y. C. Jang, Y.-H. Choa and W.-H. Yeo, *Nat. Commun.*, 2020, **11**, 3450.
22 S. Kaenphakdee, S. Yodyingyong, J. Leelawattanachai, W. Triampo, N. Sanpo, J. Jitputti and D. Triampo, *Mater. Sci. Forum*, 2020, **1007**, 143–147.
23 Y. Cai, H. Fan, M. Xu and Q. Li, *Colloids Surf., A*, 2013, **436**, 787–795.
24 A. H. Rakhsha, H. Abdizadeh, E. Pourshaban, M. R. Golobostanfard, V. R. Mastelaro and M. Montazerian, *Materialia*, 2019, **5**, 100212.
25 R. Gupta, N. KrishnaRao Eswar, J. M. Modak and G. Madras, *RSC Adv.*, 2016, **6**, 85675–85687.
26 Y. Ma, T.-W. Choi, S. H. Cheung, Y. Cheng, X. Xu, Y.-M. Xie, H.-W. Li, M. Li, H. Luo, W. Zhang, S. K. So, S. Chen and S.-W. Tsang, *Nanoscale*, 2019, **11**, 8736–8743.
27 F. A. Alharthi, A. A. Alghamdi, N. Al-Zaqri, H. S. Alanazi, A. A. Alsyahi, A. El Marghany and N. Ahmad, *Sci. Rep.*, 2020, **10**, 20229.
28 H. H. Nersisyan, J. H. Lee, J.-R. Ding, K.-S. Kim, K. V. Manukyan and A. S. Mukasyan, *Prog. Energy Combust. Sci.*, 2017, **63**, 79–118.
29 M. A. Majeed Khan, R. Siwach, S. Kumar, M. Ahmed and J. Ahmed, *J. Mater. Sci.: Mater. Electron.*, 2020, **31**, 6360–6371.
30 J. Kazmi, P. C. Ooi, S. R. A. Raza, B. T. Goh, S. S. A. Karim, M. H. Samat, M. K. Lee, M. F. Mohd, R. Wee, M. F. M. Taib and M. A. Mohamed, *J. Alloys Compd.*, 2021, **872**, 159741.
31 C.-F. Tang, S. A. Kumar and S.-M. Chen, *Anal. Biochem.*, 2008, **380**, 174–183.
32 J. Liu, T. Xu, X. Sun, J. Bai and C. Li, *J. Alloys Compd.*, 2019, **807**, 151652.
33 R. Suresh, K. Giribabu, R. Manigandan, A. Stephen and V. Narayanan, *RSC Adv.*, 2014, **4**, 17146.
34 Y. Mei, Y. Lu, F. Polzer, M. Ballauff and M. Drechsler, *Chem. Mater.*, 2007, **19**, 1062–1069.
35 X. Kong, H. Zhu, C. Chen, G. Huang and Q. Chen, *Chem. Phys. Lett.*, 2017, **684**, 148–152.